

Modeling the Evolution of the Atmospheric Boundary Layer Coupled to the Land Surface for Three Contrasting Nights in CASES-99

G. J. STEENEVELD, B. J. H. VAN DE WIEL, AND A. A. M. HOLTSLAG

Meteorology and Air Quality Group, Wageningen University, Wageningen, Netherlands

(Manuscript received 16 September 2004, in final form 12 July 2005)

ABSTRACT

The modeling and prediction of the stable boundary layer over land is a persistent, problematic feature in weather, climate, and air quality topics. Here, the performance of a state-of-the-art single-column boundary layer model is evaluated with observations from the 1999 Cooperative Atmosphere–Surface Exchange Study (CASES-99) field experiment. Very high model resolution in the atmosphere and the soil is utilized to represent three different stable boundary layer archetypes, namely, a fully turbulent night, an intermittently turbulent night, and a radiative night with hardly any turbulence (all at clear skies). Each archetype represents a different class of atmospheric stability. In the current model, the atmosphere is fully coupled to a vegetation layer and the underlying soil. In addition, stability functions (local scaling) are utilized based on in situ observations.

Overall it is found that the vertical structure, the surface fluxes (apart from the intermittent character) and the surface temperature in the stable boundary layer can be satisfactorily modeled for a broad stability range (at a local scale) with the current understanding of the physics of the stable boundary layer. This can also be achieved by the use of a rather detailed coupling between the atmosphere and the underlying soil and vegetation, together with high resolution in both the atmosphere and the soil. This is especially true for the very stable nights, when longwave radiative cooling is dominant. Both model outcome and observations show that in the latter case the soil heat flux is a dominant term of the surface energy budget.

1. Introduction

After sunset with clear skies, the surface starts to cool due to longwave radiation emission, and consequently the atmospheric boundary layer (ABL) becomes stably stratified. Understanding the physics of the stable boundary layer (SBL) is relevant to weather forecasting (Viterbo et al. 1999), climate modeling (Holtslag and Boville 1993), air quality modeling (Neu 1995), and CO₂ budget studies (Pattey et al. 2002). In this study we focus on the nighttime stable boundary layer, although the daytime is also considered to some extent.

Three distinct physical processes mainly govern the evolution and the structure of SBL: turbulence, radiative cooling, and the interaction of the SBL with the vegetation and the underlying soil. Additional features

such as gravity waves, drainage flows, katabatic flows, density currents (Sun et al. 2003a), downward transport of residual-layer turbulence, and processes related to spatial heterogeneity are also relevant (Mahrt 1987, 1999; Mahrt et al. 1998; Acevedo and Fitzjarrald 2001), besides advection and thermodynamic processes including water vapor.

One of the following three SBL archetypes may occur, depending on the relative importance of radiation and turbulence: 1) fully turbulent, 2) intermittently turbulent, and 3) radiative SBL (van de Wiel et al. 2003, hereafter W03). The very stable boundary layer, as defined by Mahrt et al. (1998), includes the intermittent and radiative archetypes. Wind shear is dominant during a continuously turbulent night, and radiative flux divergence and the soil heat flux dominate during the radiative archetype. The intermittent archetype consists of alternating dominance of turbulence and radiative flux divergence. The challenge is to develop an ABL model that is able to predict all three archetypes.

Current large-scale models encounter serious problems with SBL modeling (see section 2; Beljaars 1995;

Corresponding author address: Dr. G. J. Steeneveld, Meteorology and Air Quality Group, Wageningen University, Duivendaal 2, 6701 AP Wageningen, Netherlands.
E-mail: Gert-Jan.Steeneveld@wur.nl

Beljaars and Viterbo 1998; Holtslag 2003; Cuxart et al. 2005). On one hand, the process descriptions of the physics can be inaccurate or incomplete. On the other hand, more resolution than is currently used may be needed to solve the SBL. If the latter is true, then to what physical process (turbulence, radiation, or soil and vegetation) is more allocation of computational effort needed to achieve the best results?

The aim of this paper is to answer the question whether the SBL can be satisfactorily modeled when resolution in both the atmosphere and the soil is not a limiting factor. Therefore, we evaluate the performance of a single-column model for all three SBL archetypes (fully turbulent, intermittently turbulent, and radiative) at high vertical resolution as a proof of principle. We will in particular explore the modeling of soil and vegetation because the soil heat flux is a relatively large component of the surface energy budget during nighttime. We will compare our results with observations from the extensive 1999 Cooperative Atmosphere–Surface Exchange Study (CASES-99) dataset (Poulos et al. 2002).

In section 2, background information and additional motivation for the present study is given. In section 3, the observational data is examined, including the surface energy budget closure. Section 4 describes the model configuration, and section 5 presents the results. Conclusions are drawn in section 6.

2. Background

Current SBL parameterizations in large-scale numerical weather prediction (NWP) and climate models encounter problems with predicting the near-surface atmospheric structure (Beljaars and Holtslag 1991; Betts et al. 1998; Derbyshire 1999; Chen et al. 2004). Turbulence transport parameterizations in these models are based on similarity theory (McVehil 1964; Oke 1970; Businger et al. 1971; Louis 1979; Kot and Song 1998; Howell and Sun 1999). However, the prerequisites of homogeneity and stationarity for applying similarity theory are often not met for very stable conditions (e.g., Cauchy et al. 1979). Several studies report a significant model bias of predicted surface fluxes for very stable conditions (Carson and Richards 1978; Delage 1997; Louis 1979; Poulos and Burns 2003).

For very stable (weak wind) conditions and during the day–night transition, radiative flux divergence significantly influences the SBL structure (mainly by decreasing the inversion strength) in governing the atmospheric cooling rate near the surface as shown by Funk (1960), André and Mahrt (1982), Garratt and Brost (1981, hereafter GB81), Nkemdirim (1978, 1988), Gopalakrishnan et al. (1998), and discussed by Andreas

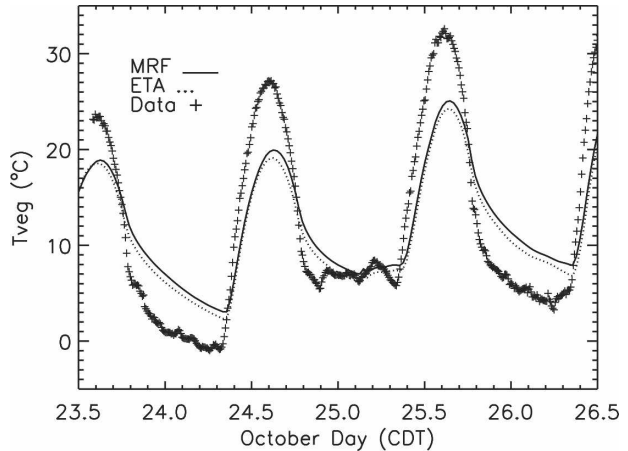


FIG. 1. Estimated vegetation surface temperature using the MM5 with the MRF (full line) and ETA (dashed line) boundary layer scheme, compared with CASES-99 observations (+), (23–26 Oct 1999).

(2002). The coupling between the lower atmosphere and the land surface is of major importance, especially under very stable conditions (Deardorff 1978; Best 1998; van de Wiel et al. 2002a,b).

As an illustration of current parameterization problems in meso- and large-scale models for stable conditions, we analyze a typical result of a mesoscale model [fifth-generation Pennsylvania State University–National Center for Atmospheric Research (PSU–NCAR) mesoscale model (MM5), version 3.5, with U.S. Geologic Survey (USGS) land use classification] for the CASES-99 campaign for 23–26 October 1999. We use both the first-order closure model with prescribed diffusion profile form, medium-range forecast (MRF) (Hong and Pan 1996), and a 1.5-order TKE- l closure model, ETA (Janjić 1990). Horizontal resolution is set to 1 km for the innermost grid nest (in total three nested grids were used), and 30 vertical model layers were used, 20 of which are located in the lowest 600 m. The European Centre for Medium-Range Weather Forecasts (ECMWF) operational analysis provided the initial and boundary conditions every six hours.

In general, the model results for both turbulence schemes agree with each other. The model overestimates the wind speed near the surface and near-surface stability is underestimated at night. The modeled surface temperature is several degrees too high (Fig. 1), especially for the weak wind nights (first and third night). Furthermore, the intermittent character observed in the turbulent fluxes in the first night is absent in both model versions. This example from a typical state-of-the-art mesoscale model shows a clear discrepancy with local observations, even at high horizontal and vertical resolution. Similar discrepancies are found by

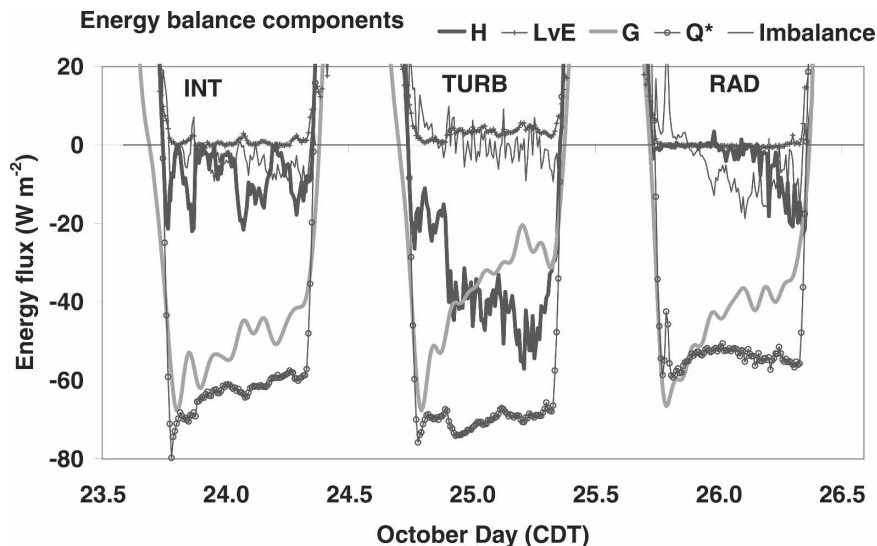


FIG. 2. Surface energy partitioning for the period of 23–26 Oct 1999 for CASES-99; H is the sensible heat flux (full black line), L_vE is the latent heat flux (thin black line with pluses), G is the soil heat flux (thick gray line), and Q^* is the net radiation (thin black line with open circles). The first night is classified as intermittent, the second as fully turbulent, and the last as radiative.

Hanna and Yang (2001) and Zhong and Fast (2003) with MM5 and Viterbo et al. (1999) for routine use of NWP.

Besides the impact of turbulent diffusion, observations indicate that the soil heat flux is extremely important during nighttime (W03), especially during weak winds since the turbulent fluxes are then small or absent (Fig. 2). Figure 2 also shows that, if the sensible heat flux changes, the soil heat flux reacts immediately on a similar time scale as the change of the sensible heat flux. We conclude that special attention to the coupling of the atmosphere and the surface is necessary (Dear-dorff 1978; Derbyshire 1995, 1999; Best 1998; van de Wiel 2002a; Steeneveld et al. 2005).

Although we expect three-dimensional models to consider advection and effects of spatial heterogeneity better than a single-column model (SCM), the parameterization problems in large-scale models mentioned above motivated us to use a SCM with state-of-the-art physics for turbulent diffusion, longwave radiation transfer, and coupling of the atmosphere with the vegetation and the soil. Several SCM studies on the SBL were performed in the past, but many of them are limited to weak stratification with a strong geostrophic wind \mathbf{V}_g . For example, Brost and Wyngaard (1978) modeled a SBL with $\mathbf{V}_g = 10 \text{ m s}^{-1}$ with prescribed surface temperature as a boundary condition. In this manner, however, the dynamic interaction with the soil and the vegetation is not considered. In addition, radiative flux divergence was neglected, which is only allowed for large wind speed (e.g., Steeneveld et al. 2005).

Similar SCM studies (i.e., without radiative flux divergence and/or prescribed surface temperature) were performed by Nieuwstadt and Driedonks (1979), Delage (1974), Mailhot and Benoit (1982), Basu and Raghavan (1986), and Sharan and Gopalakrishnan (1997) with similar results. Finally, Galmarini et al. (1998) found good agreement between large-eddy simulations (LES) and their SCM for large \mathbf{V}_g .

Recently, Rama Krishna et al. (2003) extended the former studies by simulating three different wind regimes: strong winds, moderate winds, and weak winds. They used a detailed radiation transfer model and 1.5-order turbulence closure. However, they also prescribed the surface temperature; consequently, the interdependence of the surface temperature and the sensible and soil heat fluxes were not considered.

Tjemkes and Duynkerke (1989, hereafter TD89) simulated SBLs with strong and moderate \mathbf{V}_g . With a narrow-band model for longwave radiation transfer and a force–restore method at the surface, they obtained good agreement with the Cabauw tower and energy budget observations.

Duynkerke (1991, hereafter D91), Musson-Genon (1987), Vogelesang and Holtslag (1996), Steeneveld et al. (2005), and others recognized the vital role of the interaction with the surface and coupled the atmosphere to the surface with either a bulk conductance layer or a force–restore method.

To summarize, former studies generally concentrated on the modeling of fully turbulent nights with a strong

mechanical forcing [allowing radiative flux divergence to be neglected safely, e.g., Estournel and Guedalia (1985)] and typically surface temperatures were prescribed. Since the atmosphere–land surface coupling is essential for SBL evolution, it will be emphasized in this study.

3. Observational data

In this paper, CASES-99 observations are used to validate the model. The CASES-99 measurement campaign was organized to study the relevant processes in the SBL and to improve SBL model parameterizations (Poulos et al. 2002). The experiment was conducted near Leon, Kansas (37.6486°N, −96.7351°E, 436 m MSL) and lasted from 1 to 31 October 1999. The area consisted of relatively flat homogeneous terrain (average slopes are 0.2°) with a relatively dry soil and lacks obstacles in the near surroundings. The roughness length for momentum (z_0) was 0.03 m.

Ground-based observations consist of profiles of temperature, humidity, and wind along a 60-m mast and turbulent and radiative fluxes near the surface. The eddy-covariance measurements of the surface sensible heat flux (H) and friction velocity (u_*) were obtained at 2.6 m. Because the soil heat flux (G) becomes a key process during strong stability, special emphasis was given to the observations of this quantity by using simultaneous information of the temperature at 3 and 8 cm below the surface and soil heat flux plates at 5.4 cm depth (W03). We fitted a Fourier series (150 components to account also for the high frequency changes—without fitting the noise—as is shown below) through the 3-cm data and determined the soil diffusivity (κ) by translating this series to the 8-cm level. Consequently, the soil temperature $T_s(z, t)$ is known. Here we assumed a homogeneous soil since no spatial information on the soil structure is available. In reality, soil properties may vary in space considerably.

Differentiating $T_s(z, t)$ with respect to z and substituting $z = 0$ provides the surface soil heat flux G_0 (for details see W03; Heusinkveld et al. 2003; van Wijk and de Vries 1963).

The surface energy budget (SEB) closure is rather good for all selected nights (Fig. 3), especially considering that nighttime turbulent fluxes are often small and hence difficult to measure accurately. The closure provides confidence in the observations for comparison with the model.

Hourly launched radiosondes provided information on the structure of temperature, wind speed, and direction above 60 m AGL. Wind speed structure below 200 m was obtained with sodar. (The data are available at <http://www.atd.ucar.edu/rtf/projects/cases99/asciiDownload.jsp>.)

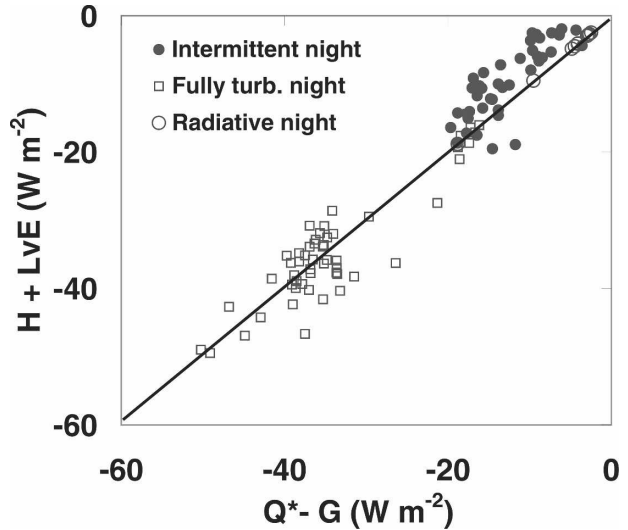


FIG. 3. The closure of the observed surface energy balance for the night (0000–0600 CDT) for 23–24 (intermittent night), 24–25 (continuous turbulent night), and 25–26 (radiative night) Oct during CASES-99.

The observed vegetation surface temperature (T_{veg}) was determined from the apparent radiation temperature T_{IRT} from the observed longwave up- and downwelling radiation, assuming an emissivity of $\epsilon = 0.98$, both for dry grass and the underlying soil (Oke 1978). With the vegetation covering a fraction of the surface, $f_{veg} = 0.9$ (based on visual inspection of the field), we obtain for T_{veg} :

$$\sigma T_{IRT}^{4.5} = \epsilon f_{veg} \sigma T_{veg}^{4.5} + \epsilon (1 - f_{veg}) \sigma T_{s0}^{4.5}, \quad (1)$$

with σ the Stefan–Boltzmann constant. We use a 4.5 power law because we are observing in the atmospheric window where the integral over the Planck curve $B(\lambda)$ can be approximated with $M = \int_{\lambda_1}^{\lambda_2} B(\lambda) = cT^b$ for a certain temperature range. In this expression c is a proportionality constant and $b = 4.5$ (not 4) in this case (H. A. R. de Bruin 2005, personal communication).

We selected three consecutive clear nights, 23–24, 24–25, and 25–26 October 1999 (Fig. 2, Table 1). Each night was classified as one of the archetypes discussed in section 1. The first night is intermittently turbulent, with several turbulent mixing events (Sun et al. 2003a). Banta et al. (2002) reports a low-level jet (LLJ) with mean speed of 7.6 m s^{-1} , typically at a height of 100 m (see their Table 2). The 0200 central daylight time (CDT) radiosonde shows a LLJ of 12 m s^{-1} at 100 m. In the second (turbulent) night, a continuous LLJ with mean wind speed of 15.2 m s^{-1} and the LLJ altitude increased during the night. Mahrt and Vickers (2002) show that local friction velocity is obviously higher at 60 m than near the ground. They qualify this SBL as an

TABLE 1. Micrometeorological conditions on the three selected nights (23–24, 24–25, and 25–26 Oct) averaged over 0000–0600 CDT for type: intermittent (Int), turbulent (Turb), and radiative (Rad).

Date (Oct 1999)	Type	u_* (m s^{-1})	U_{10} (m s^{-1})	T_{10} (K)	Q^* (W m^{-2})	H (W m^{-2})	$L_v E$ (W m^{-2})	G (W m^{-2})
23–24	Int	0.069	2.9	275.02	–61.2	–9.1	0.5	–48.3
24–25	Turb	0.300	6.28	282.11	–69.6	–43.4	3.9	–29.5
25–26	Rad	0.023	2.02	285.29	–53.4	–2.9	–0.3	–39.6

upside down boundary layer and suggest advection and mesoscale circulations are important during this night (section 4e). The last (radiative) night has a mean 10-m wind speed of only 2.0 m s^{-1} and a mean LLJ speed of 3.8 m s^{-1} . The mean LLJ height is not well defined.

The surface sensible heat flux shows an intermittent character during the first night, is relatively constant, has a large magnitude during the second night, and vanishes during most of the last night. For all nights G is a relatively large component in the energy budget, with a clear maximum (in absolute sense) just after the day–night transition and a gradual increase during the night (Fig. 2).

4. Model description

The single-column model used here is basically developed by Duynkerke (1991) to solve the governing equations for the atmosphere for an incompressible horizontal homogeneous flow (Stull 1988; Garratt 1992). The model combines the detailed calculation of turbulence, heat transfer by longwave radiation, soil and surface processes, and thus includes a detailed description of the main physical processes. For this study in particular the surface scheme is updated (section 4c)

a. Turbulence

The turbulent mixing of momentum and heat is local (e.g., Duynkerke and de Roode 2001),

$$\overline{w'X'} = -K_x \frac{\partial X}{\partial z}, \quad (2)$$

where X is a mean quantity and X' is its fluctuating part. The eddy diffusivity K_x is given by first-order closure (D91; Holtslag 1998),

$$K_x = \frac{l^2}{\phi_m \phi_x} \left| \frac{\partial \mathbf{V}}{\partial z} \right| \quad x \in \{m, h, q\}, \quad (3)$$

with $l = kz$ and $x = m, h,$ and q for momentum, heat and humidity, respectively, and k is the von Kármán constant (taken as 0.4). D91 proposes, after reanalysis of Cabauw observations in Nieuwstadt (1984),

$$\phi_x(\zeta) = \frac{kz}{X_*} \frac{\partial \bar{X}}{\partial z} = 1 + \beta_x \zeta \left(1 + \frac{\beta_x}{\alpha_x} \zeta \right)^{\alpha_x - 1}$$

$$x \in \{m, h, q\}, \quad (4)$$

with $\zeta = z/\Lambda$ in which Λ the local Obukhov length is defined by $\Lambda = -\bar{\theta} u_{*L}^3 / (kgw'\theta')$, with u_{*L} the local friction velocity. We use a priori $\beta_m = \beta_h = 5$ (Businger et al. 1971) and $\alpha_m = \alpha_h = 0.8$ (D91). This a priori choice gives reasonable agreement with CASES-99 observations, at least for $z/\Lambda < 2$. Figure 4 shows the ϕ_x functions inferred from analysis of mean profiles from CASES-99 (see the appendix) for momentum (a) and heat (b) together with proposals by Dyer (1974) and Beljaars and Holtslag (1991). The ϕ_m agrees with the results of Klipp and Mahrt (2004) for CASES-99. Note that the uncertainty for ϕ_h is larger than that for ϕ_m (e.g., Andreas and Hicks 2002), both increasing with stability. Note that we apply ϕ_h for humidity as well.

b. Radiation

Several studies show the relevance of radiative flux divergence on the structure and development of the SBL (Garratt and Brost 1981; André and Mahrt 1982). We utilize the graybody emissivity model by GB81 (and used by D91), which considers the absorbing effects of water vapor, CO_2 , and liquid water. In this scheme, each specific layer emits radiation to other layers with a single emissivity that depends on the amount of absorber between the specific layer and the other layers.

Ha and Mahrt (2003) found the vertical resolution to be a key issue for the radiation transfer model performance. A fine grid spacing ($\sim 1 \text{ m}$ near the surface) is required to estimate the longwave radiative divergence accurately. With a coarse resolution, radiative cooling near the ground is negligibly small or the model even predicts radiative warming.

Earlier studies (e.g., Tjemkes 1988) showed that the output from several emissivity models can differ (approximately 10 W m^{-2}) from those of line-by-line models near the surface (Gopalakrishnan et al. 1998), the latter giving the most accurate results. However, the graybody approach is computationally more efficient;

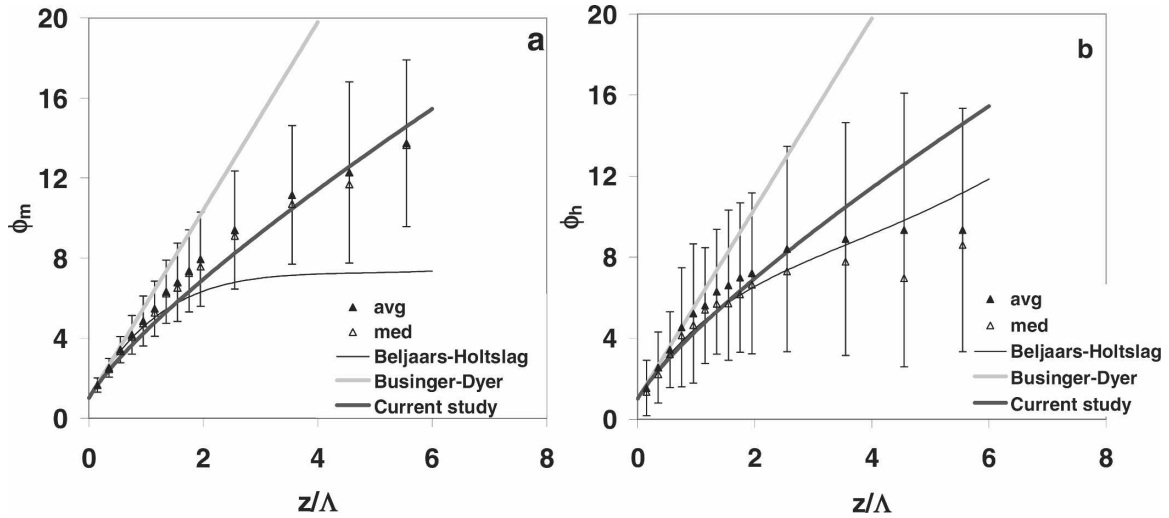


FIG. 4. Observed dimensionless gradients of (a) wind speed and (b) potential temperature as function of local stability (z/Λ) for CASES-99. Filled triangles are mean values, open triangles are median values for the CASES-99 observations. Full lines are the proposals by Businger-Dyer (Dyer 1974; gray line), Beljaars and Holtslag (1991; thin black line), and the curve used in the current model (thick black line).

therefore, we prefer the graybody approach in this study.

c. Soil and vegetation surface

Figure 5 depicts the structure of the land surface scheme and the definitions of the various temperatures: T_{veg} is the vegetation surface temperature, T_{s0} is the soil surface temperature just below the vegetation, T_d is the soil temperature 75 cm below the soil surface, and $T_s(z)$ is the soil temperature at a level z below the surface.

The diffusion equation gives the evolution of the soil temperature (T_s),

$$\frac{\partial T_s}{\partial t} = \kappa \nabla^2 T_s, \tag{5}$$

with κ the soil diffusivity for heat ($m^2 s^{-1}$). The soil heat flux, $G(z)$ is then given by

$$G(z) = -\lambda \frac{\partial T_s}{\partial z}, \tag{6}$$

where λ is the soil conductivity ($\lambda = 0.6 W m^{-1} K^{-1}$ estimated from the CASES-99 observations, W03). Note that λ and κ depend on soil moisture content. However, the observed soil moisture content was relatively constant during the three-day period considered here, and therefore we use constant values for λ and κ . A conductance law parameterizes the soil heat flux at the surface, G_0 :

$$G_0 - (1 - f_{veg})K^\downarrow = r_g(T_{veg} - T_{s0}), \tag{7}$$

where K^\downarrow is the incoming shortwave radiation ($W m^{-2}$) at the surface, f_{veg} is the fraction of the soil surface covered by vegetation, and r_g is the conductance for heat transport between the vegetation layer and the soil surface.

Figure 6 shows the empirical conductance law of Eq. (7) for CASES-99 observations for both daytime and nighttime. With $f_{veg} = 0.9$, we estimate $r_g = 5.9 W m^{-2} K^{-1}$ (from the slope in Fig. 6). Note the relatively large scatter due to the empirical character of Eq. (7). D91 found $r_g = 3.0 W m^{-2} K^{-1}$ and Holtslag and de Bruin (1988) obtained $r_g = 5 W m^{-2} K^{-1}$ for Cabauw. Thus, the current value is in reasonable agreement with other observations for grass. A better fit through the data is obtained by $G_0 - (1 - f_{veg})K^\downarrow = \gamma(T_{veg} - T_{s0}) + \mu(T_{veg} - T_{s0})^2$ with $\gamma = 5.4$ and $\mu = 0.11$.

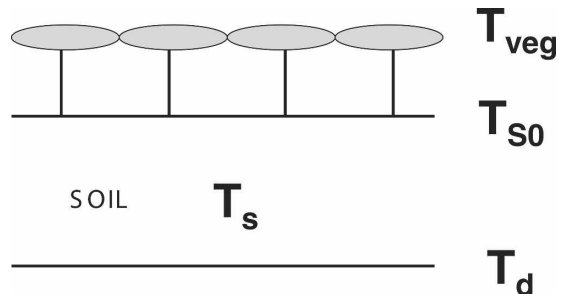


FIG. 5. Illustration of the model setup of the vegetation and land surface; T_{veg} is the vegetation surface temperature, T_{s0} is the soil surface temperature, and T_d is the deep soil temperature at 75 cm in the soil.

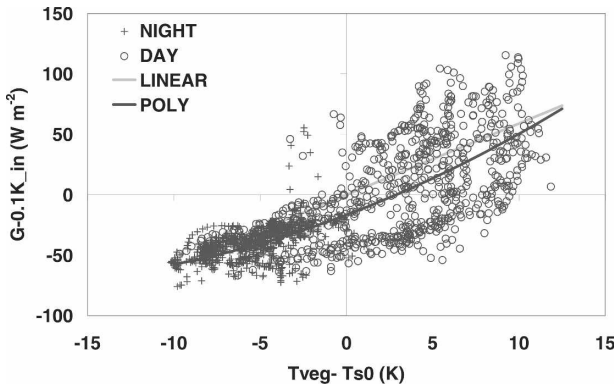


FIG. 6. Observed relationship between the soil heat flux and the temperature difference between the vegetation surface temperature and the soil surface temperature. Open circles are data with daytime observations, pluses are nighttime observations (based on incoming solar radiation). The black thick line is a quadratic fit through the observations and the gray thick line is a linear regression through the observations [see text, Eq. (7)]. The slope of the curve indicates the bulk conductance.

However, this more complex form only slightly improved the nighttime model results compared to Eq. (7).

The vegetation surface temperature (T_{veg}) follows from the SEB:

$$C_v \frac{\partial T_{veg}}{\partial t} = Q^* - G - H - L_v E, \quad (8)$$

where C_v is the heat capacity of the vegetation per unit area, Q^* is the vegetation surface net radiation, $L_v E$ the latent heat flux. D91 found $C_v = 2 \times 10^4 \text{ J m}^{-2} \text{ K}^{-1}$ for Cabauw, while W03 used $C_v = 2000 \text{ J m}^{-2} \text{ K}^{-1}$ for CASES-99 (and is used here).

Measurements (section 2) show that both T_{veg} and T_{s0} experience rapid changes, which indicate that relatively high temporal frequencies play a vital role in the soil heat dynamics (W03; Heusinkveld et al. 2003). The modeled G should be able to reproduce these fast dynamics and therefore the model requires fine vertical spatial resolution to resolve this. Consequently, we add a homogenous soil of 0.75 m (150 layers with a vertical resolution of $\Delta z = 0.005 \text{ m}$). Of course, in practice one could save computing time by using a logarithmic spacing near the surface. The soil diffusivity $\kappa = 0.155 \times 10^{-6} \text{ m}^2 \text{ s}^{-1}$ (as found by W03), soil density 1850 kg m^{-3} and its heat capacity $2150 \text{ J kg}^{-1} \text{ K}^{-1}$. We apply no explicit scheme for soil moisture.

d. Grid structure

To account for the large gradients of wind speed, temperature, and humidity near the surface we use a

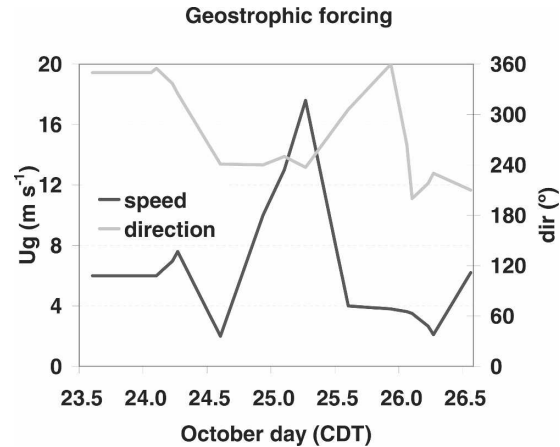


FIG. 7. Graphical representation of the geostrophic wind speed (black line) and direction (gray line) obtained from radiosondes during CASES-99 for 23–26 Oct 1999. These observations are used to force the model.

logarithmic grid spacing with $\Delta z \sim 0.5 \text{ m}$ close to the surface and $\Delta z \sim 60 \text{ m}$ at the model top (1800 m):

$$Z = \frac{z}{A} + \ln\left(\frac{z+B}{B}\right). \quad (9)$$

Here Z is the level of the grid points and z the actual height. We choose $A = 200 \text{ m}$, $B = 1 \text{ m}$. The first model level is located at 0.30 m . The model results are quite insensitive to the exact location of the first model level. A fine grid mesh is not specifically required for turbulent flux calculation [due to the compensating effects already indicated by Delage (1988)], but is necessary for the radiation transfer model (Ha and Mahrt 2003).

e. Initial conditions

The initial profiles for wind speed, temperature and humidity are obtained from the radiosonde observations at the CASES-99 central site 1400 CDT 23 October 1999. At that time, the potential temperature in the convective boundary layer is constant up to 800 m .

The geostrophic wind \mathbf{V}_g to force the model was derived from a series of radiosonde observations (usually available every 3 h) at the CASES-99 central site at 800 m above ground level (Fig. 7). Based on the observations it is felt that the impact of baroclinicity was relatively small, so it is neglected and \mathbf{V}_g is taken constant with height. Above $z = 1000 \text{ m}$ we prescribe the wind speed equal to \mathbf{V}_g .

From the CASES-99 observations we estimated $z_0 = 0.03 \text{ m}$ (W03; Sharan et al. 2003) and we apply $z_{0h} = z_0/10$ for the roughness length for heat (Garratt 1992). The canopy resistance was set constant at 1400 s m^{-1} to

TABLE 2. Bias, root-mean-square error (rmse), and median of the error between model results for the period (0000–0600 CDT) and observations separated per night, types as in Table 1.

	Bias			Rmse			Median		
	23–24 Int	24–25 Turb	25–26 Rad	23–24 Int	24–25 Turb	25–26 Rad	23–24 Int	24–25 Turb	25–26 Rad
H (W m^{-2})	5.0	−7.6	2.6	9.0	9.4	6.8	6.5	−7.8	2.4
$L_v E$ (W m^{-2})	−1.7	−1.1	−0.3	1.9	1.4	0.68	−1.9	−1.1	−0.15
G_0 (W m^{-2})	−0.24	−2.4	−1.8	3.3	3.2	3.8	−0.07	−3.0	−1.26
T_{veg} (K)	−0.74	1.1	0.01	0.84	1.2	0.57	−0.74	1.1	0.16
u_* (m s^{-1})	−0.076	−0.015	−0.030	0.09	0.04	0.055	−0.07	−0.017	−0.019
RH (2 m) (%)	2.4	−7.1	−18.3	2.3	7.8	19.8	2.3	8.0	−18.1
Q^* (W m^{-2})	0.74	−7.6	−10.0	1.9	7.9	10.8	0.6	−6.8	−11.0
L^\downarrow (W m^{-2})	−2.8	−5.5	−10.8	2.9	5.9	11.2	−2.8	−6.1	−10.7
L^\uparrow (W m^{-2})	−3.6	2.1	−0.89	3.9	2.8	2.7	−3.6	2.3	0.0b

represent the very dry soil at the end of the growing season.

We used the observed values of initial vegetation surface temperature $T_{\text{veg}} = 296.1$ K, the initial soil surface temperature $T_{s0} = 292.6$ K, and the deep soil temperature at $z = 0.75$ m in the soil $T_d = 286.6$ K. The initial soil temperature profile was imposed $T_s(z, t = 0) = \max(283.0, T_{s0} - A\sqrt{z})$ K with $A = 16 \text{ K m}^{-1/2}$. In this manner, the deep soil temperature matches the observed 288.0 K at 0.08 m and the T_s is uniform below 0.36 m. The lower boundary condition is a constant T_d of 283 K. The longwave incoming radiation at the model top was taken from climatological values from Cerni and Parish (1984, their Fig. 5) and amounts to 250 W m^{-2} .

f. Advection

The SCM approach requires prescription of advective tendencies. We determined the temperature advection rate from a mesoscale analysis of radiosondes in a network around the CASES-99 site. All sites are typically at 250 km distance from the CASES-99 site: Norman, Oklahoma (OUN), Dodge City, Kansas (DDC), Topeka, Kansas (TOP), and Springfield, Missouri (SGF). We found $5 \times 10^{-5} \text{ K s}^{-1}$ for the temperature advection at the boundary layer top for the period between 1400 CDT 24 October and 1400 CDT 25 October and negligibly small advection for the rest of the period. From a mesoscale analysis with MM5, we found approximately the same value for temperature advection. This advection is prescribed to the whole model domain except for the lowest 100 m where the advection decreases linearly to zero at the surface.

Visual inspection of the inversion above the convective boundary layer from radiosondes provided the subsidence rate about $\sim 0.5 \times 10^{-3} \text{ m s}^{-1}$ during the first 48 h and zero during the last 24 h.

5. Results and discussion

This section provides model results in comparison with CASES-99 observations with a focus on surface fluxes, surface vegetation temperature, and vertical profiles of temperature and wind speed during nighttime. Note that the model is only initialized once and that the total run comprises three full days. Table 2 summarizes the bias, root-mean-square error (rmse) and median of the error between model and observations for a number of surface variables.

a. Surface fluxes

The diurnal cycle of the modeled net radiation Q^* agrees with the observations (not shown). Net radiation amounts typically $Q^* = 400 \text{ W m}^{-2}$ during daytime and $Q^* = -70 \text{ W m}^{-2}$ during nighttime. For the second (turbulent) night and the second part of the third (radiative) night, the magnitude of Q^* is somewhat underestimated (7.6 W m^{-2} on average). This is caused by the overestimated longwave incoming radiation (L^\downarrow ; Fig. 8a). A first explanation for this overestimated L^\downarrow is that the model is slightly too humid and too warm (next section), which increases the atmospheric emissivity and consequently L^\downarrow . A second possible explanation is that the real (unknown) L^\downarrow at the model top can be larger than the imposed climatological value. The relative impact of radiative cooling is largest just during the day–night transition (not shown), which agrees with Funk (1960), Ha and Mahrt (2003), and Sun et al. (2003b). Outgoing longwave radiation, L^\uparrow is simulated correctly during the whole period, which implies an accurate simulation of the surface vegetation temperature (see also Fig. 8e).

The evolution of the friction velocity (u_*) is shown in Fig. 8b. The friction velocity decrease during the sunset preceding the first (intermittent) night is simulated

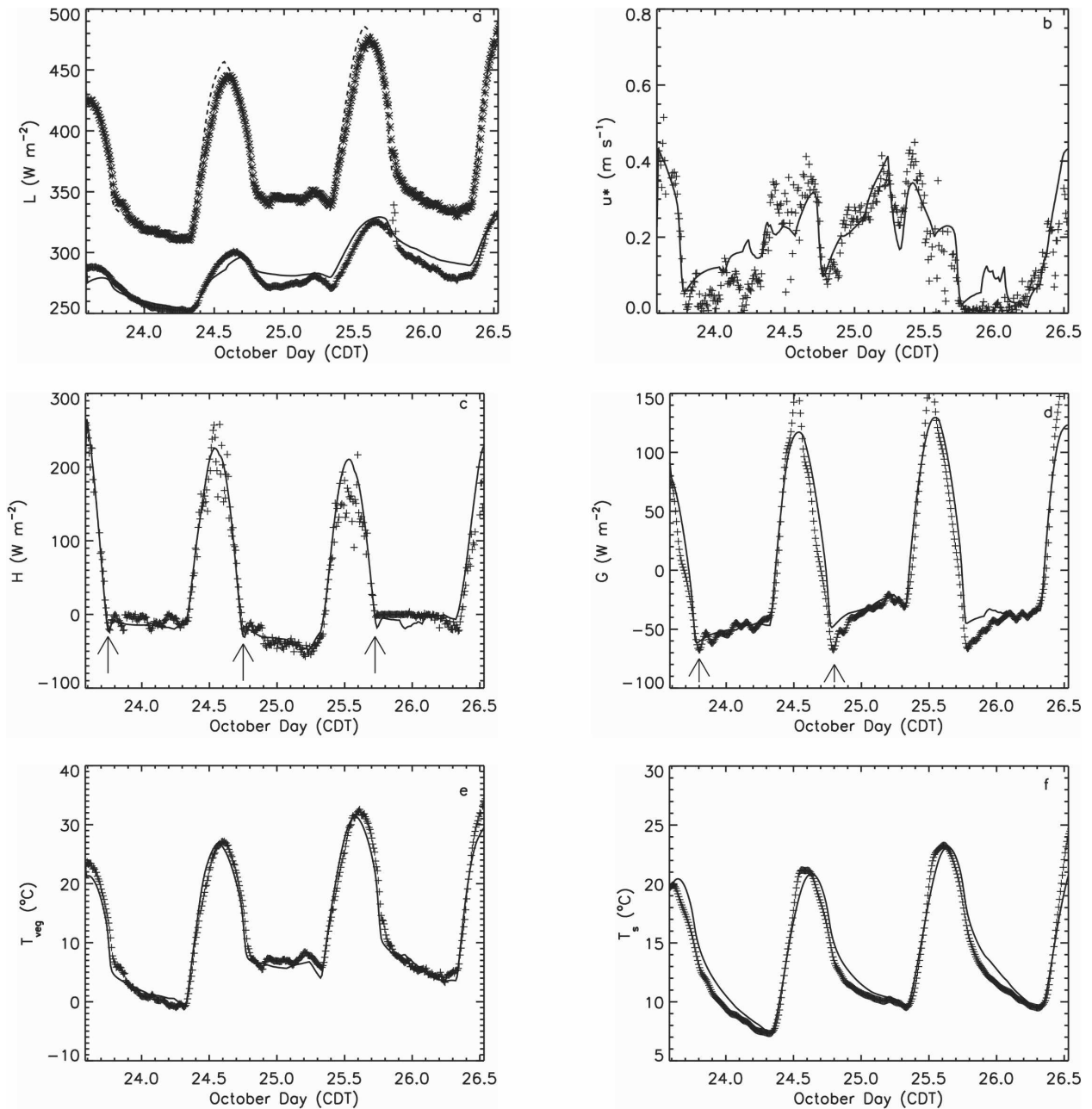


FIG. 8. (a) Time series of observed (+) and simulated (continuous line) downward longwave radiation and observed (*) and simulated (dashed line) upward longwave radiation at $z = 10$ m AGL for the three nights during CASES-99. (b) Time series of observed (+) and simulated (continuous line) surface friction velocity. As in (b) but for (c) sensible heat flux, (d) soil heat flux, (e) vegetation surface temperature, and (f) soil surface temperature.

rather well, although the bias amounts 0.076 m s^{-1} over the whole night. The model lacks a clear turbulence collapse as observed during the first (intermittent) night. The cause of this overestimated u_* can either be due to the slightly underestimation of the fitted ϕ_m in the stability range of $1 < z/\Lambda < 3$ (Fig. 4a), or the imposed \mathbf{V}_g is larger than the real \mathbf{V}_g . In the period

0700 CDT 24 October–1700 CDT 25 October the model performs well, while during the last (radiative) night u_* is slightly too high until midnight but follows the collapse at the end of the night. The overall bias amounts to 0.03 m s^{-1} for the last night. Sodar observations show much smaller wind speeds at 200 m AGL (which is above the SBL during this night) than the

imposed \mathbf{V}_g . This may suggest that \mathbf{V}_g was overestimated, and this consequently may explain the bias in u_* . In general it is known that models correctly predict u_* for strong winds but overestimate u_* for weak winds (TD89; Sharan and Gopalakrishnan 1997).

The maximum sensible heat flux amounts approximately 250 W m^{-2} during daytime (Fig. 8c) close to the observations. In the first (intermittent) night, the modeled $H = -14.1 \text{ W m}^{-2}$ on average, while -9.1 W m^{-2} was observed. However, the model does not simulate the observed intermittent character of the surface fluxes (Fig. 2). In contrast, the conceptual model by van de Wiel et al. (2002a) was able to simulate and predict intermittent turbulence and was, as such, supported by observations. However, owing to their highly simplified model, this can only be regarded more suggestive of intermittent SBL behavior rather than a definitive answer. Some models with more resolution (ReVelle 1993; Welch et al. 1986) were also able to reproduce intermittent turbulence. On the other hand, the models by Sharan and Gopalakrishnan (1997) and Derbyshire (1999) did not show any intermittency. The current model is regarded as a more realistic physical model than the conceptual model by van de Wiel et al. (2002a), with high resolution instead of a bulk scheme and with a more detailed soil and radiation scheme. A sensitivity study was performed (not shown) to investigate whether intermittency could be found in a certain part of the parameter space. A total collapse of the turbulence and even a small oscillation was found. However, this was not convincing evidence to state that the current model is able to represent intermittency, at least for the given case. This subject needs further investigation.

Just after the day–night transition to the intermittent night, the observed magnitude of H shows a clear maximum (see arrows in Fig. 8c), which is well reproduced by the model. This maximum is caused by a sudden reversal of the stratification near the surface due to longwave radiation emission during the day–night transition, and is maintained by residual turbulence of the convective boundary layer. This is an often observed realistic feature [e.g., during 11 of the 30 nights for CASES-99 and in the First International Satellite Land Surface Climatology Project (ISLSCP) Field Experiment (FIFE) observations shown by Chen and Dudhia (2001)]. However, most modeling studies rarely show these minima. The reproduction of this detailed feature emphasizes the realism of the model outcome.

During the turbulent night (24–25 October), the predicted H follows the observations. The specific minimum during the day–night transition (1900 CDT 24 October) is present here as well. Radiative flux divergence dominates the last (radiative) night and the observed H

is approximately zero. The model slightly overestimates the magnitude of H (-2.9 W m^{-2}), mainly caused by an overestimation of u_* . This causes a weaker stratification and thus a larger magnitude of H . The second half of this night the model gives good results.

The actual latent heat flux was small since the observed soil moisture content was low. The daytime Bowen ratio was ~ 5 , which underlines the dry conditions. The latent heat flux shows a diurnal cycle with maxima of $\sim 50 \text{ W m}^{-2}$ during daytime and negligibly small evapotranspiration during nighttime ($|L_v E| < 10 \text{ W m}^{-2}$). The model satisfactorily simulates this (Table 2) with hardly any bias and small rmse.

The model predicts G_0 accurately except for a negative bias during noon (Fig. 8d). During nighttime, we find a bias of -0.2 , -2.4 , and -1.4 W m^{-2} for the three nights, respectively. As mentioned above, G_0 is a relatively dominant term in the SEB (about -50 W m^{-2}) and has fast dynamics; that is, a sharp maximum of the magnitude of G_0 is seen soon after the day–night transition. TD89 also found this sharp maximum of the magnitude of G_0 , although with a smaller frequency than found here. The fast dynamics are evidently important for the SBL development and are modeled correctly. This maximum occurs at the day–night transition, because the vegetation surface cools rapidly since the radiative forcing is largest at that moment. To compensate for the strong cooling, the magnitude of G_0 rapidly increases. Later on, the surface cooling rate is smaller because net radiative cooling diminishes (TD89; Poulos and Burns 2003). As indicated above, the current model does not simulate intermittency in this case, thus no oscillations are present in the simulated G_0 either.

As mentioned in the introduction, a common problem for large-scale models is to provide a reliable prediction of T_{veg} (see also section 2). Some models show unphysical decoupling of the atmosphere from the surface resulting in so-called runaway cooling of T_{veg} (Sorteberg 2002). On the other hand, the pragmatic enhanced mixing approach, which is commonly used for very stable conditions, leads to overestimation of T_{veg} . Figure 8e shows the results for T_{veg} and Fig. 8f for T_{s0} for the current study. For both daytime and nighttime, T_{veg} is simulated in very good agreement with the data, despite the fact that we cover a broad range of stability. Model bias amounts to -0.7 , 1.1 , and 0.0 K , respectively, for the three nights. This is a surprising result given that T_{veg} is usually hard to predict, even with an offline model (Best 1998).

In summary, we conclude that the present model generates surface fluxes that are in good agreement with observations because of the detail in the descrip-

tion of the surface scheme, the soil heat flux, and radiation physics (with high resolution).

b. Vertical profiles

Figures 9a–c show representative examples of observed and simulated instantaneous temperature profiles along the 60-m mast for the three nights. For the intermittent night (Fig. 9a), the agreement is reasonable, although the modeled curvature is less than observed. For the second (continuous turbulent) night (Fig. 9b) the temperature profile is represented very well. Both model results and observations show a strong curvature during the radiative night (Fig. 9c) with a surface inversion of about 13 K in the lowest 60 m. We can attribute satisfactory modeling to the radiation transport model, which takes over the heat transport in a natural way when turbulence vanishes. After the turbulence vanishes, the model does not show any kind of so-called runaway cooling. Negative feedbacks in Q^* (decreasing in response to surface cooling) as in G_0 (increasing magnitude in response to surface cooling) compensate for absence of turbulence in a natural way. This clearly underlines the fact that a radiation transfer model is required, preferably with a high vertical resolution near the surface. The current model also satisfactorily reproduces the results of Estournel and Guedalia (1985) for $\mathbf{V}_g = 3 \text{ m s}^{-1}$ (not shown).

Figures 10a–c show measured (along the mast and from sodar) and modeled wind speed profiles. Sodar and mast observations agree well with each other, although they have been measured at a horizontal distance of approximately 2 km. During the first (intermittent) night (Fig. 10a), the modeled and observed wind speed profiles agree fairly well. During the fully turbulent night (Fig. 10b) with a wind speed of 9 m s^{-1} at 60 m, the wind profile estimate is in good agreement below $z = 60 \text{ m}$. Above this level, the LLJ is clearly seen by sodar observations, but is underestimated in the model (see also Mailhot and Benoit 1982). Lack of vertical resolution to resolve a LLJ cannot explain this deficiency here. Baroclinicity can play a role in the development or sharpening of the LLJ in reality (Stull 1988) while we neglect baroclinicity in our SCM approach.

During the third (radiative) night, the observed wind is very weak. In the beginning of the night (before 0200 CDT), the modeled wind speed is too large, probably related to the fact that our imposed \mathbf{V}_g was larger than \mathbf{V}_g in reality. In this period, the observed wind speed profile was decoupled from the surface over a layer $\sim 20 \text{ m}$ thick. The model is not able to capture this decoupled boundary layer and overestimates the wind speed. Model results compare well with sodar observa-

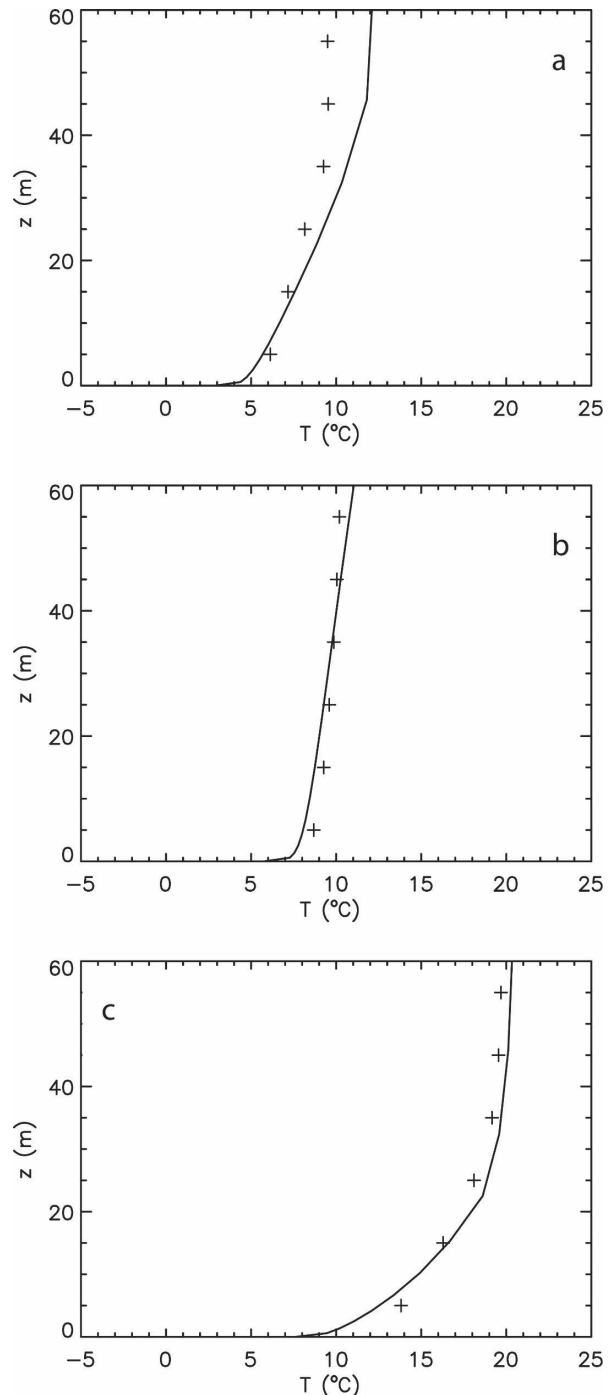


FIG. 9. Observed (+) and simulated (line) temperature profiles for (a) 0100 CDT 24 Oct (intermittent night), (b) 0100 CDT 25 Oct (continuous turbulent night), and (c) 2300 CDT 25 Oct (radiation night).

tions for the shown profile, which is representative for the period 0200–0500 CDT. A weak LLJ (3.5 m s^{-1} , 25 m AGL) was observed, although the model underestimates its strength. Mast measurements clearly depart

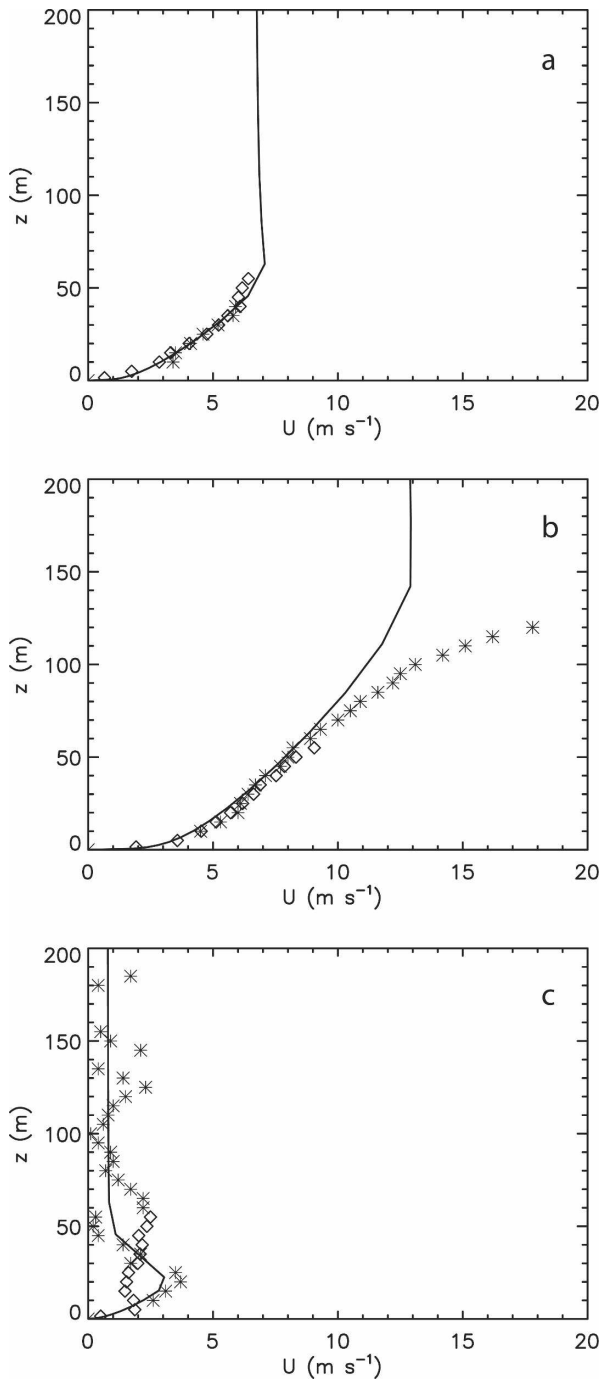


FIG. 10. As in Fig. 9 but for wind speed. Diamonds denote the most observations and stars the sodar observations.

from sodar observations. With these weak winds, the SBL structure differs on small spatial scales. In addition, we approach the anemometer measurement accuracy. Specific humidity profiles show reasonable agreement (maximum bias 0.5 g kg^{-1} , not shown) except just before 0000 CDT 26 October when a temporary accu-

mulation of humidity appears (bias of $+1.5 \text{ g kg}^{-1}$) and a negative specific humidity gradient.

In general, the model is able to estimate temperature and wind profiles except for the night that is purely driven by radiative cooling when the decoupled wind profiles could not be modeled correctly. In their intercomparison study, Sharan and Gopalakrishnan (1997) found that mean profiles become insensitive to the type of closure for very stable conditions. The diffusion in these conditions is so small that differences in diffusion are hardly seen in the mean profiles. This underlines that processes other than turbulent diffusion become more important when the wind drops.

Figures 11a–c show the characteristic calculated total cooling subdivided in the radiative cooling and the turbulent cooling as function of height for the three nights at 0200 CDT. Both turbulent and radiative cooling profiles are well defined for the first two nights, with strong radiative cooling near the surface. Cooling profiles are comparable with those in TD89, who used a line-by-line radiation transfer model and with the results in Gopalakrishnan et al. (1998). For the last night we note that the cooling rates are large, especially considering the fact that the boundary layer is thin. Radiative cooling is less well defined with warming between $z = 10$ and 20 m , while the turbulent cooling is much stronger (large flux divergence despite small fluxes). The radiative warming is caused by the local accumulation of humidity in the lowest model levels (below $z = 50 \text{ m}$) where $dq/dz < 0$. Below $z = 5 \text{ m}$, dq/dz decreases and the radiation transfer model predicts cooling.

c. Sensitivity to initial conditions

To examine the robustness of the results, we performed some sensitivity analysis on the initial conditions and model parameters. Disturbing the initial temperature (by 1 K), wind profiles (by 5%), soil temperature, and vegetation temperature (both by 1 K) do not affect the results seriously. In addition, reinitialization the model every 24 hours (1400 CDT) with observed radiosonde information showed hardly any impact on the results (not shown).

6. Conclusions

The aim of this paper has been to investigate whether the stable boundary layer can be satisfactorily modeled over a broad range of atmospheric stability with the current understanding of the stable boundary layer physics. Therefore, we have studied the development of the atmospheric boundary layer over land for a three-day period including three different archetypes for stable conditions. These archetypes are (i) a fully tur-

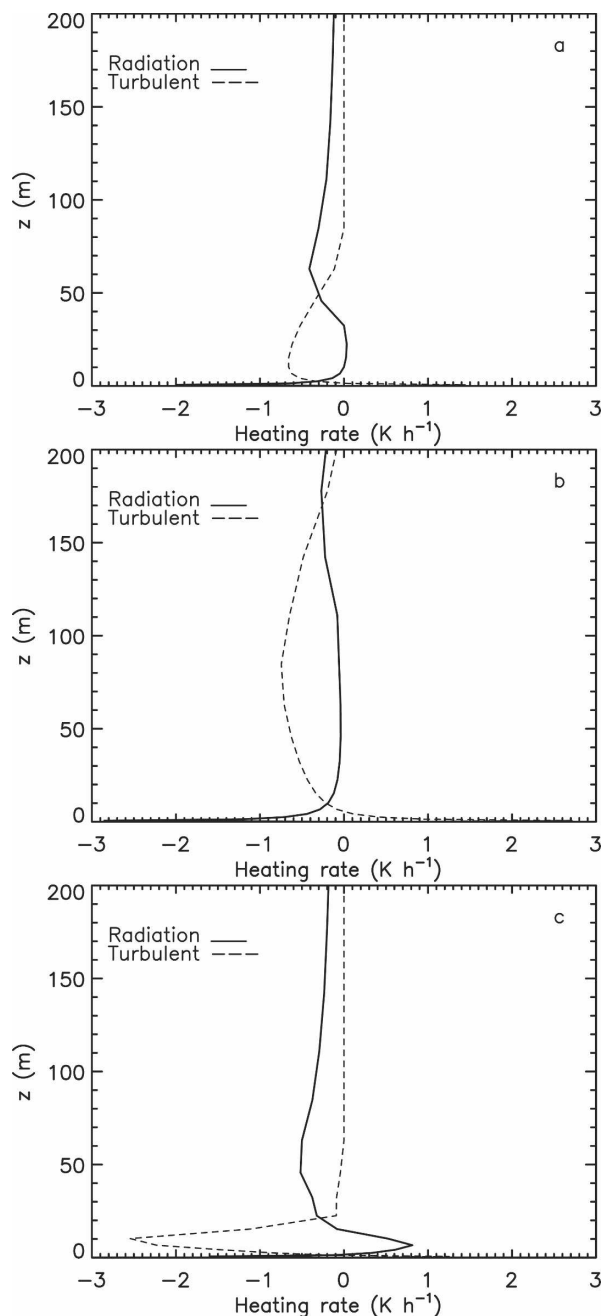


FIG. 11. Vertical profiles of estimated turbulent (full line) and radiative cooling (dashed line) for (a) 0100 CDT 24 Oct (intermittent night), (b) 0100 CDT 25 Oct (continuous turbulent night), and (c) 0200 CDT 26 Oct (radiation night).

bulent night, (ii) an intermittently turbulent night, and (iii) a radiation-driven night. To ensure vertical resolution was not a limiting issue, we use very high resolution in both the atmosphere and the soil. We compare single-column model results with CASES-99 observations. Contrary to many former single-column models

studies that prescribed the surface temperature, the current model solves the diffusion equation for heat in the soil and a detailed coupling between the soil and a vegetation layer. Furthermore, we use stability functions directly based on then local observations (which are well in agreement with previous ones)

We find that the vertical structure, the surface fluxes, and the surface temperature in the stable boundary layer can be satisfactorily modeled (at least at a local scale) with our current understanding of the physics of the stable boundary layer for a broad stability range. This can be achieved by the use of a detailed coupling between the atmosphere and the underlying soil and vegetation together with high resolution in both the atmosphere and the soil. These results are surprisingly good, certainly given the problematic feature regarding the parameterization of the stable boundary layer in large-scale models and the fact that, in our case, the model was initialized only once for the three-day period examined.

Features that are not captured by the current model are the intermittent nature of the surface fluxes during the intermittent night and the sharp low-level jet in the turbulent night (the latter is related to the one-dimensional model character). Nevertheless, we have shown that a state-of-the-art boundary layer model coupled to the vegetation and underlying soil, without limitations to the amount of vertical resolution in the soil and the atmosphere, is able to reproduce the CASES-99 observations. In a future study, we plan to explore the sensitivity of the model formulations to vertical resolution in more detail and to extend our findings for applications on a larger scale.

Acknowledgments. The authors acknowledge all the scientists involved in the CASES-99 experiment, in particular Oscar Hartogensis and Henk de Bruin for gathering and processing the surface fluxes used in this study. We also thank Peter Baas for his contribution on the flux–profile relationships for CASES-99. Our colleague Leo Kroon is acknowledged for his valuable comments on the manuscript. We are indebted to our late colleague Peter Duynkerke, since many of our findings are achieved by using his model code with all its innovative aspects (Duynkerke 1991). Finally, Jordi Vilà is acknowledged for providing this code.

APPENDIX

Estimating the Flux Profile Relationships for CASES-99

To cover the broad stability range in this study (Figs. 4a and 4b), the classical Businger–Dyer flux profile re-

relationships (Businger et al. 1971) are extended from the weakly SBL ($z/\Lambda < 1$) to $z/\Lambda = 7$ with data from the CASES-99 experiment. Thermocouples and anemometers are located at $z = 5, 15, 25, \dots, 55$ m and sonic anemometers at $z = 1.5, 5, 10, 20, \dots, 50$ and 55 m and were considered with 5-min intervals. We estimate vertical gradients with an extension of the log-linear function (Nieuwstadt 1984),

$$X = A + Bz + Cz^2 + D \ln z, \quad (\text{A1})$$

with $X = \theta$ or U . Alternatives for A1 are given in Akima (1970), Oncley et al. (1996), Frenzen and Vogel (2001), or Johansson et al. (2001). The variability of the gradients from these methods is within 20% of the estimate for $z > 10$ m, but we found a factor of 2 difference between methods near the surface. Only the log-linear profile and Eq. (A1) can capture large gradients near the surface. We restricted ourselves to data points with $d\theta/dz > 0.025 \text{ K m}^{-1}$; $dU/dz > 0.025 \text{ s}^{-1}$; $1.5 < z < 50$ m; and $\overline{w'\theta'} < -0.005 \text{ K m s}^{-1}$. Nights that were classified as radiative by W03 were excluded.

REFERENCES

- Acevedo, O. C., and D. R. Fitzjarrald, 2001: The early evening surface layer transition: Temporal and spatial variability. *J. Atmos. Sci.*, **58**, 2650–2667.
- Akima, H., 1970: A new method of interpolation and smooth curve fitting based on local procedures. *J. Assoc. Comp. Mach.*, **17**, 589–602.
- André, J. C., and L. Mahrt, 1982: The nocturnal surface inversion and influence of clear-air radiative cooling. *J. Atmos. Sci.*, **39**, 864–878.
- Andreas, E. L., 2002: Parameterizing scalar transfer over snow and ice: A review. *J. Hydrometeorol.*, **3**, 417–432.
- , and B. B. Hicks, 2002: Comments on “Critical test of the validity of Monin–Obukhov similarity during convective conditions.” *J. Atmos. Sci.*, **59**, 2605–2607.
- Banta, R. M., R. K. Newsom, J. K. Lundquist, Y. L. Pichugina, R. L. Coulter, and L. Mahrt, 2002: Nocturnal low-level jet characteristics over Kansas during CASES-99. *Bound.-Layer Meteorol.*, **105**, 221–252.
- Basu, S., and N. Raghavan, 1986: Prediction of inversion strengths and heights from a 1-D nocturnal boundary layer model. *Bound.-Layer Meteorol.*, **35**, 193–204.
- Beljaars, A. C. M., 1995: The impact of some aspects of the boundary layer scheme in the ECMWF model. *Proc. Seminar on Parametrization of Sub-grid Scale Physical Processes*, Reading, United Kingdom, ECMWF, 125–161.
- , and A. A. M. Holtslag, 1991: Flux parameterization over land surfaces for atmospheric models. *J. Appl. Meteorol.*, **30**, 327–341.
- , and P. Viterbo, 1998: Role of the boundary layer in a numerical weather prediction model. *Clear and Cloudy Boundary Layers*, A. A. M. Holtslag and P. G. Duynkerke, Eds., Royal Netherlands Academy of Arts and Sciences, 287–304.
- Best, M. J., 1998: A model to predict surface temperatures. *Bound.-Layer Meteorol.*, **88**, 279–306.
- Betts, A. K., P. Viterbo, and A. C. M. Beljaars, 1998: Comparison of the land–surface interaction in the ECMWF reanalysis model with the 1987 FIFE data. *Mon. Wea. Rev.*, **126**, 186–198.
- Brost, R. A., and J. C. Wyngaard, 1978: A model study of the stably stratified planetary boundary layer. *J. Atmos. Sci.*, **35**, 1427–1440.
- Businger, J. A., J. C. Wyngaard, Y. Izumi, and E. F. Bradley, 1971: Flux profile relationships in the atmospheric surface layer. *J. Atmos. Sci.*, **28**, 181–189.
- Carson, D. J., and P. J. R. Richards, 1978: Modelling surface turbulent fluxes in stable conditions. *Bound.-Layer Meteorol.*, **14**, 67–81.
- Cauchey, S. J., J. C. Wyngaard, and J. C. Kaimal, 1979: Turbulence in the evolving stable boundary layer. *J. Atmos. Sci.*, **36**, 1041–1052.
- Cerni, T. A., and T. R. Parish, 1984: A radiative model of the stable nocturnal boundary layer with application to the polar night. *J. Climate Appl. Meteorol.*, **23**, 1563–1572.
- Chen, F., and J. Dudhia, 2001: Coupling an advanced land surface–hydrology model with the Penn State–NCAR MM5 modeling system. Part II: Preliminary model validation. *Mon. Wea. Rev.*, **129**, 587–604.
- Chen, Y., F. L. Ludwig, and R. L. Street, 2004: Stably stratified flows near a notched transverse ridge across the Salt Lake Valley. *J. Appl. Meteorol.*, **43**, 1308–1328.
- Cuxart, J., and Coauthors, 2005: A single-column model intercomparison for a stably stratified atmospheric boundary layer. *Bound.-Layer Meteorol.*, in press.
- Deardorff, J. W., 1978: Efficient prediction of ground surface temperature and moisture with inclusion of a layer of vegetation. *J. Geophys. Res.*, **83**, 1889–1903.
- Delage, Y., 1974: A numerical study of the nocturnal atmospheric boundary layer. *Quart. J. Roy. Meteor. Soc.*, **100**, 351–364.
- , 1988: A parameterization of the stable atmospheric boundary layer. *Bound.-Layer Meteorol.*, **43**, 365–381.
- , 1997: Parameterising sub-grid scale vertical transport in atmospheric models under statically stable conditions. *Bound.-Layer Meteorol.*, **82**, 23–48.
- Derbyshire, S. H., 1995: Stable boundary-layer modelling: Established approaches and beyond. *Bound.-Layer Meteorol.*, **90**, 423–446.
- , 1999: Boundary layer decoupling over cold surfaces as a physical boundary instability. *Bound.-Layer Meteorol.*, **90**, 297–325.
- Duynkerke, P. G., 1991: Radiation fog: A comparison of model simulation with detailed observations. *Mon. Wea. Rev.*, **119**, 324–341.
- , and S. de Roode, 2001: Surface energy balance and turbulence characteristics observed at the SHEBA ice camp during FIRE III. *J. Geophys. Res.*, **106**, 15 313–15 322.
- Dyer, A. J., 1974: A review of flux-profile relationships. *Bound.-Layer Meteorol.*, **7**, 363–372.
- Estournel, C., and D. Guedalia, 1985: Influence of geostrophic wind on atmospheric nocturnal cooling. *J. Atmos. Sci.*, **42**, 2695–2698.
- Frenzen, P., and A. G. Vogel, 2001: Further studies of atmospheric turbulence in layers near the surface: Scaling the TKE budget above the roughness sublayer. *Bound.-Layer Meteorol.*, **99**, 173–206.
- Funk, J. P., 1960: Measured radiative flux divergence near the ground at night. *Quart. J. Roy. Meteor. Soc.*, **86**, 382–389.
- Galmardini, S., C. Beets, P. G. Duynkerke, and J. Vila-Guerau de Arellano, 1998: Stable nocturnal boundary layers: A com-

- parison of one-dimensional and large-eddy simulation models. *Bound.-Layer Meteor.*, **88**, 181–210.
- Garratt, J. R., 1992: *The Atmospheric Boundary Layer*. Cambridge University Press, 316 pp.
- , and R. A. Brost, 1981: Radiative cooling effects within and above the nocturnal boundary layer. *J. Atmos. Sci.*, **38**, 2730–2746.
- Gopalakrishnan, S. G., M. Sharan, R. T. McNider, and M. P. Singh, 1998: Study of radiative and turbulent processes in the stable boundary layer under weak wind conditions. *J. Atmos. Sci.*, **55**, 954–960.
- Ha, K. J., and L. Mahrt, 2003: Radiative and turbulent fluxes in the nocturnal boundary layer. *Tellus*, **55A**, 317–327.
- Hanna, S. R., and R. Yang, 2001: Evaluation of mesoscale models' simulations of near-surface winds, temperature gradients, and mixing depths. *J. Appl. Meteor.*, **40**, 1095–1104.
- Heusinkveld, B. G., A. F. G. Jacobs, A. A. M. Holtslag, and S. M. Berkowicz, 2003: Surface energy balance closure in an arid region: Role of soil heat flux. *Agric. For. Meteorol.*, **122**, 21–37.
- Holtslag, A. A. M., 1998: Modeling of atmospheric boundary layers. *Clear and Cloudy Boundary Layers*, A. A. M. Holtslag and P. G. Duynkerke, Eds., Royal Netherlands Academy of Arts and Sciences, 85–110.
- , 2003: GABLS initiates intercomparison for stable boundary layer case. *GEWEX News*, Vol. 13, No. 2, 7–8.
- , and H. A. R. de Bruin, 1988: Applied modeling of the nighttime surface energy balance over land. *J. Appl. Meteor.*, **27**, 689–704.
- , and B. A. Boville, 1993: Local versus nonlocal boundary-layer diffusion in a global climate model. *J. Climate*, **6**, 1825–1842.
- Hong, S. Y., and H. L. Pan, 1996: Nonlocal boundary layer vertical diffusion in a medium-range forecast model. *Mon. Wea. Rev.*, **124**, 2322–2339.
- Howell, J. F., and J. Sun, 1999: Surface-layer fluxes in stable conditions. *Bound.-Layer Meteor.*, **90**, 495–520.
- Janjić, Z. I., 1990: The step-mountain coordinate: Physical package. *Mon. Wea. Rev.*, **118**, 1429–1443.
- Johansson, C., A. Smedman, U. Högström, J. G. Brasseur, and S. Khanna, 2001: Critical test of the validity of Monin–Obukhov similarity during convective conditions. *J. Atmos. Sci.*, **58**, 1549–1566.
- Klipp, C. L., and L. Mahrt, 2004: Flux-gradient relationship, self-correlation and intermittency in the stable boundary layer. *Quart. J. Roy. Meteor. Soc.*, **130**, 2087–2103.
- Kot, S. C., and Y. Song, 1998: An improvement of the Louis scheme for the surface layer in an atmospheric modeling system. *Bound.-Layer Meteor.*, **88**, 239–254.
- Louis, J. F., 1979: A parametric model of vertical eddy fluxes in the atmosphere. *Bound.-Layer Meteor.*, **17**, 187–202.
- Mahrt, L., 1987: Grid-averaged surface fluxes. *Mon. Wea. Rev.*, **115**, 1550–1560.
- , 1999: Stratified atmospheric boundary layers. *Bound.-Layer Meteor.*, **90**, 375–396.
- , and D. Vickers, 2002: Contrasting vertical structures of nocturnal boundary layers. *Bound.-Layer Meteor.*, **105**, 351–363.
- , J. Sun, W. Blumen, T. Delany, and S. Oncley, 1998: Nocturnal boundary-layer regimes. *Bound.-Layer Meteor.*, **88**, 255–278.
- Mailhot, J., and R. Benoit, 1982: A finite-element model of the atmospheric boundary layer suitable for use with numerical weather prediction models. *J. Atmos. Sci.*, **39**, 2249–2266.
- McVehil, G. E., 1964: Wind and temperature profiles near the ground in stable stratification. *Quart. J. Roy. Meteor. Soc.*, **90**, 136–146.
- Musson-Genon, L., 1987: Numerical simulation of a fog event with a one-dimensional boundary layer model. *Mon. Wea. Rev.*, **115**, 592–607.
- Neu, U., 1995: A parameterisation of the nocturnal ozone reduction in the residual layer by vertical downward mixing during summer smog situations using sodar data. *Bound.-Layer Meteor.*, **73**, 189–193.
- Nieuwstadt, F. T. M., 1984: The turbulent structure of the stable, nocturnal boundary layer. *J. Atmos. Sci.*, **41**, 2202–2216.
- , and A. G. M. Driedonks, 1979: The nocturnal boundary layer: A case study compared with model calculations. *J. Appl. Meteor.*, **18**, 1397–1405.
- Nkemdirim, L., 1978: A comparison of radiative and actual nocturnal cooling rates over grass and snow. *J. Appl. Meteor.*, **17**, 1643–1646.
- , 1988: Nighttime surface-layer temperature tendencies with and without chinooks. *J. Appl. Meteor.*, **27**, 482–489.
- Oke, T. R., 1970: Turbulent transport near the ground in stable conditions. *J. Appl. Meteor.*, **9**, 778–786.
- , 1978: *Boundary Layer Climates*. Methuen and Co., 372 pp.
- Oncley, S. P., C. A. Friehe, J. C. Larue, J. A. Businger, E. C. Itsweire, and S. S. Chang, 1996: Surface-layer fluxes, profiles, and turbulence measurements over uniform terrain under near neutral conditions. *J. Atmos. Sci.*, **53**, 1029–1044.
- Pattey, E., I. B. Strachan, R. L. Desjardins, and J. Massheder, 2002: Measuring nighttime CO₂ flux over terrestrial ecosystems using eddy covariance and nocturnal boundary layer methods. *Agric. For. Meteorol.*, **113**, 145–158.
- Poulos, G. S., and S. P. Burns, 2003: An evaluation of bulk rib-based surface layer flux formulas for stable and very stable conditions with intermittent turbulence. *J. Atmos. Sci.*, **60**, 2523–2537.
- , and Coauthors, 2002: CASES-99: A comprehensive investigation of the stable nocturnal boundary layer. *Bull. Amer. Meteor. Soc.*, **83**, 555–581.
- Rama Krishna, T. V. B. P. S., M. Sharan, and Aditi, 2003: Mean structure of the nocturnal boundary layer under strong and weak wind conditions: EPRI case study. *J. Appl. Meteor.*, **42**, 952–969.
- ReVelle, D. O., 1993: Chaos and “bursting” in the planetary boundary layer. *J. Appl. Meteor.*, **32**, 1169–1180.
- Sharan, M., and S. G. Gopalakrishnan, 1997: Comparative evaluation of eddy exchange coefficients for strong and weak wind stable boundary layer modeling. *J. Appl. Meteor.*, **36**, 545–559.
- , T. V. B. P. S. Rama Krishna, and Aditi, 2003: Surface-layer characteristics in the stable boundary layer with strong and weak winds. *Bound.-Layer Meteor.*, **108**, 257–288.
- Sorteberg, A., 2002: The sensitivity of inversion strength to the formulation of the non-dimensional momentum and heat profiles. Norwegian Meteorological Institute, 61 pp.
- Steenefeld, G. J., B. J. H. van de Wiel, and A. A. M. Holtslag, 2005: Modelling the Arctic nocturnal stable boundary layer and its coupling to the surface. *Bound.-Layer Meteor.*, in press.
- Stull, R. B., 1988: *An Introduction to Boundary-Layer Meteorology*. Kluwer Academic Publishers, 666 pp.
- Sun, J. D., and Coauthors, 2003a: Atmospheric disturbances that generate intermittent turbulence in nocturnal boundary layers. *Bound.-Layer Meteor.*, **110**, 255–279.

- , S. P. Burns, A. C. Delany, S. P. Oncley, T. W. Horst, and D. H. Lenschow, 2003b: Heat balance in the nocturnal boundary layer during CASES-99. *J. Appl. Meteor.*, **42**, 1649–1666.
- Tjemkes, S. A., 1988: Radiative cooling in the nocturnal boundary layer. Ph.D. thesis, Wageningen University, Wageningen, Netherlands, 107 pp.
- , and P. G. Duynkerke, 1989: The nocturnal boundary layer: Model calculations compared with observations. *J. Appl. Meteor.*, **28**, 161–175.
- van de Wiel, B. J. H., R. J. Ronda, A. F. Moene, H. A. R. de Bruin, and A. A. M. Holtslag, 2002a: Intermittent turbulence and oscillations in the stable boundary layer over land. Part I: A bulk model. *J. Atmos. Sci.*, **59**, 942–958.
- , A. F. Moene, R. J. Ronda, H. A. R. de Bruin, and A. A. M. Holtslag, 2002b: Intermittent turbulence and oscillations in the stable boundary layer over land. Part II: A system dynamics approach. *J. Atmos. Sci.*, **59**, 2567–2581.
- , —, O. K. Hartogensis, H. A. R. de Bruin, and A. A. M. Holtslag, 2003: Intermittent turbulence and oscillations in the stable boundary layer over land. Part III: A classification for observations during CASES-99. *J. Atmos. Sci.*, **60**, 2509–2522.
- van Wijk, W. R., and D. A. de Vries, 1963: Periodic temperature variations. *Physics of Plant Environment*, W. R. van Wijk, Ed., Interscience, 133–138.
- Viterbo, P., A. Beljaars, J. F. Mahfouf, and J. Teixeira, 1999: The representation of soil moisture freezing and its impact on the stable boundary layer. *Quart. J. Roy. Meteor. Soc.*, **125**, 2401–2426.
- Vogelezang, D. H. P., and A. A. M. Holtslag, 1996: Evaluation and model impacts of alternative boundary-layer height formulations. *Bound.-Layer Meteor.*, **81**, 245–269.
- Welch, R. M., M. G. Ravichandran, and S. K. Cox, 1986: Prediction of quasi-periodic oscillations in radiation fogs. Part I: Comparison of simple similarity approaches. *J. Atmos. Sci.*, **43**, 633–651.
- Zhong, S., and J. D. Fast, 2003: An evaluation of MM5, RAMS, and Meso Eta at sub-kilometer resolution using the VTMX field campaign data in the Salt Lake Valley. *Mon. Wea. Rev.*, **131**, 1301–1322.